The Exoplanet Transmission Spectroscopy Imager (ETSI), a new instrument for rapid characterization of exoplanet atmospheres

Luke M. Schmidt[a], Mary Anne Limbach[a], Erika Cook[a], D. L. DePoy[a], Ryan J. Oelkers[a], J. L. Marshall[a], Landon Holcomb[a], Willians Pena[a], Jacob Purcell[a], and Enrique Gonzalez Vega[a]

[a]Department of Physics and Astronomy Texas A&M University, 4242 TAMU, College Station, TX 77843-4242 USA

ABSTRACT

The Exoplanet Transmission Spectroscopy Imager (ETSI) amalgamates a low resolution slitless prism spectrometer with custom multiband filters to simultaneously image 15 spectral bandpasses between 430 nm and 975 nm with an average spectral resolution of $R = \lambda/\Delta\lambda \sim 20$. This enables a new technique, common-path multi-band imaging (CMI), used to observe transmission spectra of exoplanets transiting bright (V<14th mag.) stars. ETSI is capable of near photon limited observations, with a systematic noise floor on par with the Hubble Space Telescope and below the Earth's atmospheric amplitude scintillation noise limit. We report the as-built instrument optical and optomechanical design, detectors, control system, telescope hardware and software interfaces, data reduction pipeline, and upcoming science observations. We discuss ETSI's science capabilities and the results of our initial April 2022 commissioning run. ETSI requires only moderate telescope apertures (~ 2 m) and is capable of characterizing the atmospheres of dozens of exoplanets per year, enabling selection of the most interesting targets for further characterization with other ground and space-based observatories.

Keywords: Exoplanets, transmission spectroscopy, multi-band filters, precision photometry, Transits

1. INTRODUCTION

The advantages of simultaneous multi-bandpass photometry were leveraged by astronomers in the mid 20th century. Early experiments with photomultiplier tubes by Walraven resulted in the Walraven five channel spectrophotometer[1] and along with other instruments such as the Danish $uvby - \beta$ five channel spectrophotometer[2] demonstrated that simultaneous measurement of multiple bands is superior to sequential observations of multiple bands when measuring relative colors of astronomical objects. Changes in seeing and transparency can still affect the recorded brightness of an object, but any variable absorption, which is grey, has the same effect on all wavelengths leaving relative color measurements unaffected if the measurements are made simultaneously. These early instruments were complex and required very stable instruments as the bandpass selection was performed by slicing a dispersed spectrum with a set of prisms. Any flexure or motion of the star in the instrument field of view could change the bandpass seen in a given channel. Other attempts involving multiple telescopes observing with different filters or multiple dichroics, filters and detectors, one for each bandpass, become unwieldy beyond only a few bandpasses due to mechanical space constraints as well as transmission losses for channels at the end of the chain of stacked dichroics.[3–6] Fortunately, recent advances in thin film coating technology have enabled the creation of filters with many bandpasses selected by a single optic and when used in both transmission and reflection enable simultaneous measurement of many more bandpasses. The instrument described in this paper measures fifteen simultaneous bandpasses, but in principle more are possible.

The Exoplanet Transmission Spectroscopy Imager (ETSI) is based on traditional slitless spectroscopy, with a novel multi-band filter to split up each spectral band to enable quick, high precision PSF fitting photometry. This is more efficient and uncomplicated compared to traditional exoplanet transmission spectroscopy, which requires binning higher resolution spectra, wavelength calibration, and spectral fitting techniques. The common

---

Further author information: (Send correspondence to L.M.S)
L.M.S.: E-mail: lmschmidt@tamu.edu, Telephone: 1 979 845 4401

path and simultaneous nature of ETSI observations mean that any instrumental or environmental common path errors, including atmospheric scintillation, are eliminated. By referencing one science target spectral band to another science target band, color changes over the course of a transit are detectable. The ETSI optical design was optimized for consistent imaging and through focus performance to minimize residual color errors during observation.

2. SCIENCE WITH THE ETSI INSTRUMENT

ETSI is designed to carry out exoplanet characterization and vetting. Specifically, this includes exoplanet spectral transmission and occultation measurements at $R = 20$ and vetting transiting exoplanet candidates (i.e. follow-up of TESS targets). Below we describe each science case and the scientific capabilities of ETSI in more detail.

2.1 Exoplanet Transmission Spectroscopy

ETSI is capable of characterizing exoplanet atmospheres by producing spectra in the visible ($430 < \lambda < 975$ nm) in 15 spectral bands (with a typical resolution of $R \approx 20$). This is comparable to the spectral resolutions reported by other transmission spectroscopy measurements, which are typically collected at higher resolutions but binned down to lower resolutions to increase SNR. The location of the ETSI spectral band filters are designed to coincide with spectral features of interest in exoplanet atmospheres. Specifically, ETSI transmission spectra measurements are sensitive to the presence of atoms (potassium and sodium), molecules (methane, water, and TiO), clouds and aerosols in the exoplanet's atmosphere.

ETSI is ideal for characterization of transiting gas-giant planets. ETSI was commissioned on the McDonald Observatory 2.1 m in early April 2022 and began science observations in June 2022. Targets for observations are currently prioritized based on host brightness, target visibility, and exoplanet density and temperature. Generally, ETSI is targeting systems that are V$\lesssim$14 mag with transit depths $\gtrsim$10 ppt. These systems are our highest priority as only a few transits per system are required to obtain sufficient SNR to construct a transmission spectra. ETSI is capable of making spectral measurements of transiting exoplanets outside this parameter space, but such measurements are likely to require many transit measurements. Once ETSI has surveyed the most accessible targets and instrument performance has been verified, operations will shift to more time consuming systems. The ultimate goal of ETSI is to build a publicly accessible catalog of dozens of uniformly measured exoplanet transmission spectra. The database will provide the means for comparative exoplanet atmosphere studies and will allow for improvement of exoplanet atmospheric models.

ETSI does not measure absolute transit depth in each spectral band, instead it measures relative transit depth. Once an image sequence is obtained on-sky using this instrument, we use a self-referencing differential photometric technique to eliminating sources of uncertainty from non-common path sources such as atmospheric scintillation, instrumental effects, and telescopic effects. To do this we reference each spectral band of the science star to another spectral band of the same science star, which differs from traditional photometric measurements made by ratioing the flux of the science target to one or more reference stars. Our initial on-sky results show that the highest precision measurements are obtained by using a spectral band near the middle of the ETSI spectral range as our reference band. This self-referential photometry eliminates nearly all common-path systematics and allows for a differential photometric precision on the order of $10 - 25$ ppm.[7]

These self-referenced differential measurements serve as a proxy for the measured atomic and molecular features in the exoplanet's atmosphere. These features can be modeled and the atmospheric composition of the planetary atmosphere can be inferred. Spectral band referencing is used to reduce systematics in the transmission lightcurves and is a proven technique for exoplanet light curve analysis to reduce systematic noise sources.[8,9] Residual systematics can be removed with typical detrending techniques (i.e. polynomial detrending or Gaussian process regression[10–12]) in combination with time-averaged light curves from reference stars in the field of view. The best fit exoplanet atmospheric model can then be found by using standard exoplanet atmospheric retrieval tool kits, specifically the open source `python` code `petitRADTRANS`[13,14] in combination with the `emcee` Markov Chain Monte Carlo framework.[15]

Figure 1 shows a simulated ETSI spectrum of HAT-P-44b (black error bars) and several possible spectral models (gray, light blue and dark blue lines). ETSI provides sufficient sensitivity to differentiate between the
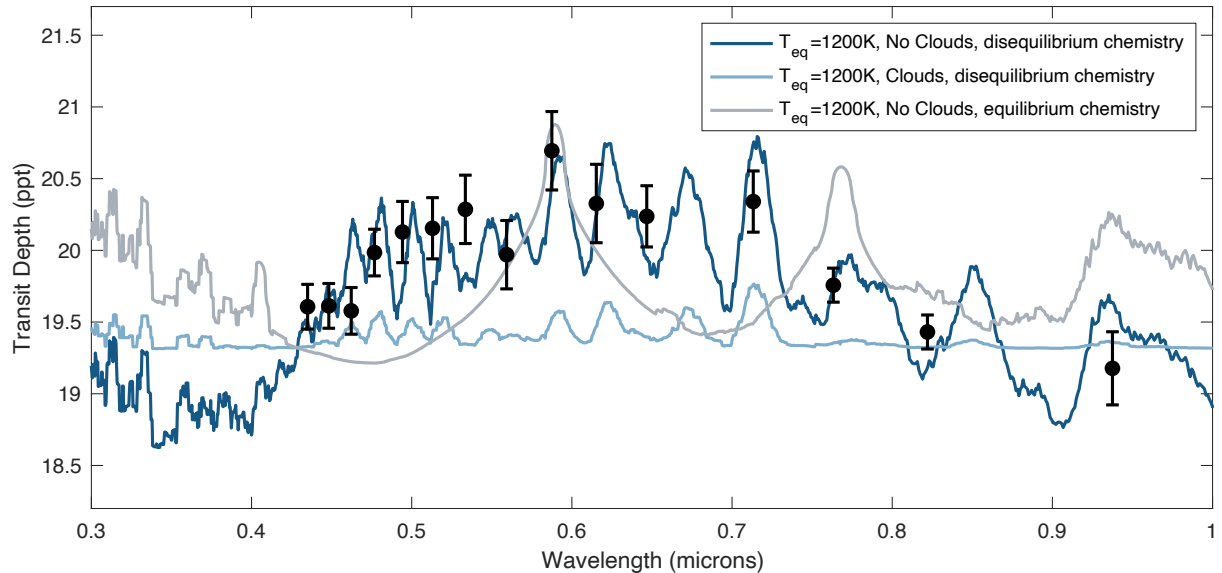
Figure 1: A simulated ETSI transmission spectra of HAT-P-44b (black error bars) and modeled transmission spectra (gray, light blue and dark blue lines) using `Exotransmit`.[16] Here the dark blue model is preferred with a strong confidence ($> 7\sigma$) over the other two models.

spectral models – in this simulation the dark blue model is preferred with a strong confidence ($> 7\sigma$) over the other models.

2.1.1 Occultation Spectroscopy

In addition to transmission spectroscopy, ETSI is also capable of measuring the change in system flux, between spectral bands, during occultation of an exoplanet or other low-mass companions (such as brown dwarfs). This provides an emission spectrum of the companion using the same self-referencing differential photometric color technique as described above. Companion temperatures are much colder than the host, and thus the largest occultation depth can be expected in ETSI's reddest spectral band (940 nm), similar to z-band but slightly narrower and redder. However, in some cases it should be possible to measure the companion's emission in multiple spectral bands. One example of this would be TOI-2119b, a brown dwarf eclipsing a M-dwarf. For this system ETSI can detect the absence of the companion's emission during occultation in most spectral bands. Figure 2 shows the emission from the brown dwarf is measurable in 6 of 8 of ETSI's transmitted spectral bands.

2.2 TESS TOI Follow-up

Current attempts from ground-based observatories to identify and rule out eclipsing (sub-)stellar companions require either multiple observations of the host star at quadrature using medium-to-high resolution spectroscopy, or multiple observations of the host star in multiple spectral bands to identify changes in the system's color during both the transit and eclipse. Unfortunately, these observations can be plagued by significant noise from the detector, achromatic sky background, instrument flexure, non-common path errors, stellar activity, and atmospheric scintillation which can produce systematics which are difficult to de-couple from the true exoplanet signatures.[19]

ETSI is also capable of vetting these objects. ETSI is able to measure color changes during eclipses in these systems. The colors can be used to derive a temperature of the companion to quickly identify stellar companions in the TESS Object of Interest (TOI) data set, as described below. This provides an means to quickly identify stellar impostors in TOI database, and avoid more expensive radial velocity follow-up.
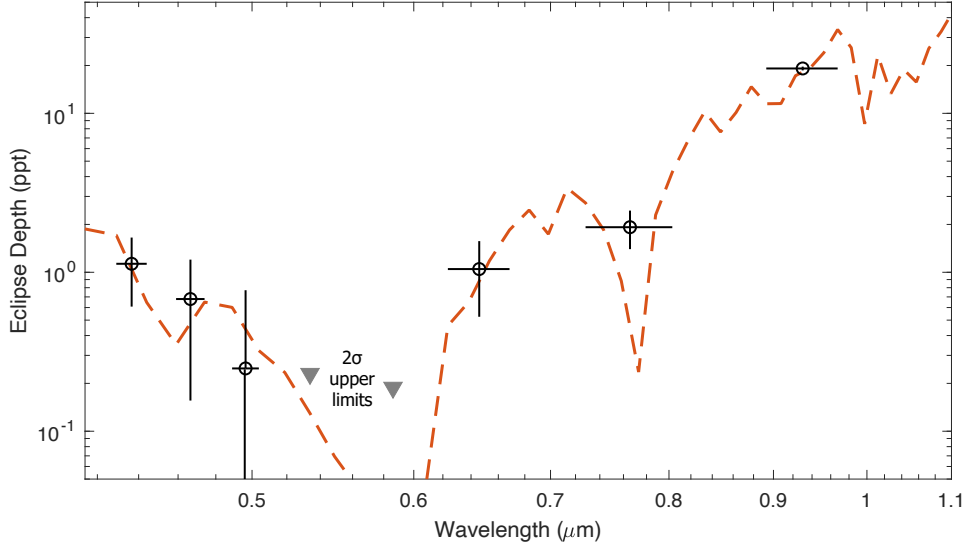
Figure 2: Simulated ETSI emission spectrum of TOI-2119b based on a single occultation measurement (black error bars; only ETSI's 8 transmitted bands are shown here) and modeled brown dwarf emission spectrum (red dashed line). ETSI occultation spectroscopy can be used to constrain the temperature of the companion and characterize its emission spectrum. Brown dwarf and M-dwarf models were used for this calculation.[17, 18]

In practice this can be done by referencing the color change in ETSI's reddest band (940 nm; which is most sensitive to cold companions) to a bluer band (e.g. 600 nm; where emission from the colder companion is less or negligible). The average host flux to average companion flux are then given by

$$E_{940-600nm} = F_{in}/F_{out} = \frac{(F'_{940nm}/F'_{600nm})_{in}}{(F'_{940nm} + F''_{940nm})_{out}/(F'_{600nm} + F''_{600nm})_{out}} \tag{1}$$

where $E_{940-600nm}$ is the differential eclipse color, F_{in} is the flux during eclipse, F_{out} is the flux out-of-eclipse, F' is the flux of the host, and F'' is the flux from the companion. We simulated our ability to differentiate between exoplanets and more massive companions (brown dwarfs and low-mass stars). The expected detection limits are shown in Figure 3 for a variety of companion temperatures.

The ratio of the companion flux to the host flux, which is equivalent to the in-eclipse to out-of-eclipse flux, is converted to an expected companion temperature by using several sets of theoretical models including: a grid of atmospheres for exoplanets and cold brown dwarfs;[17] models specific for hot brown dwarfs and cool stars;[18] and models specific for stars.[22] The best fit model is found using a least-squares method if there is only a measurable eclipse depth in the 940 nm bandpass, or using the `petitRADTRANS` package to perform a spectral retrieval on the companion if multiple bandpass measurements are available.[13, 14] These simulations suggest the measured companion temperature from a single eclipse can distinguish between stellar and sub-stellar objects orbiting bright host stars ($V < 8$) and provide an avenue to distinguish between sub-stellar and planetary objects down to a temperature of 1400 K. These eclipse measurements also provide, at minimum, an upper limit on the effective temperature of the TOI companion. ETSI could use this technique to differentiate between (sub-)stellar companions for about 1200 TOIs in total (where $T < 14.6 \approx V < 14$; $T_{\text{eff}} < 6000$ K) given sufficient observing time.

3. OPTICAL DESIGN

Typically, exoplanet transmission spectroscopy is conducted using high-resolution spectroscopic instruments on large ground and space-based observatories. These instruments are not specialized for the specific task of obtaining exoplanet transmission spectra, and are, perhaps unsurprisingly, sub-optimal for the task. Specifically,
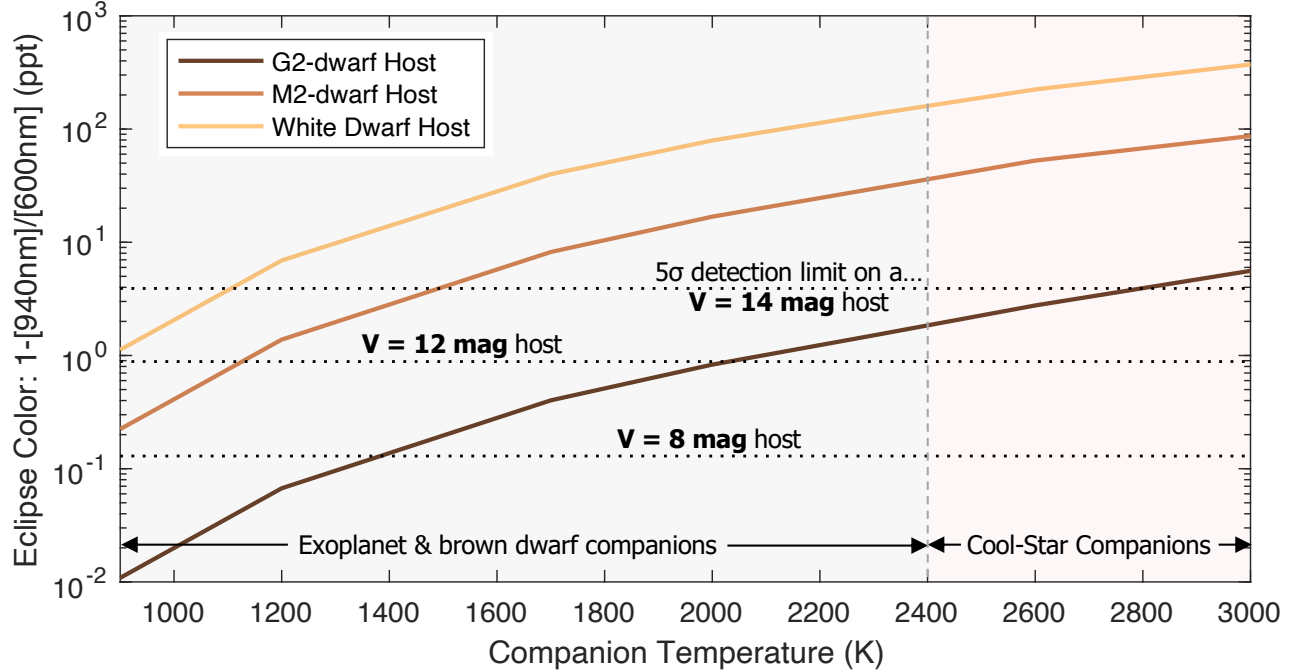
Figure 3: Simulated eclipse colors expected to be observed during the companion's eclipse for a white dwarf (yellow line), M2 (red line), and G2 (brown line) host star compared to the temperature of the companion object. The dotted lines show a detection threshold of 5σ for a $V = 8$, 12 and 14 mag host star. These simulated colors suggest stellar, brown dwarf, and exoplanet companions could be distinguished down to a temperature of 1400 K after observations of a single companion eclipse for bright ($V < 8$) host stars. For this calculation, all companions are assumed to have a radius of $1R_{Jup}$ and use band-integrated fluxes based on modeled spectra.[20, 21]

there is typically substantial room for improvement in the instrument transmission and systematic errors. Data reduction processes can be greatly eased (thereby decreasing systematic errors) by building an instrument that produces isolated, binned spectral measurements rather than needing to extract, calibrate and bin high spectral resolution data. ETSI is a purpose built instrument designed specifically to reduce systematic errors and produce high photometric precision exoplanet transmission spectra. The requirements considered throughout the optical design process are listed below.

1. Optimization wavelengths 430-975 nm: Wavelength coverage was driven by coverage of modeled exoplanet atmospheric features and constrained by the sensitivity of the ETSI detectors.

2. Compatible with $f/8$ or slower telescopes: We envisioned ETSI traveling to multiple telescopes (for example, both Northern and Southern hemisphere telescopes) and this ensured compatibility with a variety of potential telescopes.

3. Moderate focal reduction: The dispersed nature of the ETSI images mean that each band covers a fairly large number of pixels, which would be exacerbated by use at any telescope with a large focal ratio. Focal reduction also increases the field of view to increase the likelihood of comparison stars which may be useful during data reduction.

4. Imaging quality sufficient to ensure seeing limited performance: This also ensures that any residual color, or minor focus changes affect the PSF of each filter band ∼equally.

5. Maintain the angle of the multi-chroic at 30° or less: driven by the difficulty of designing the multiband filters at higher angles of incidence.

6. Maintain at least 20 mm of distance between the final camera optical element and the focal plane: This is a reasonable distance that was compatible with the majority of currently available cameras that were considered.

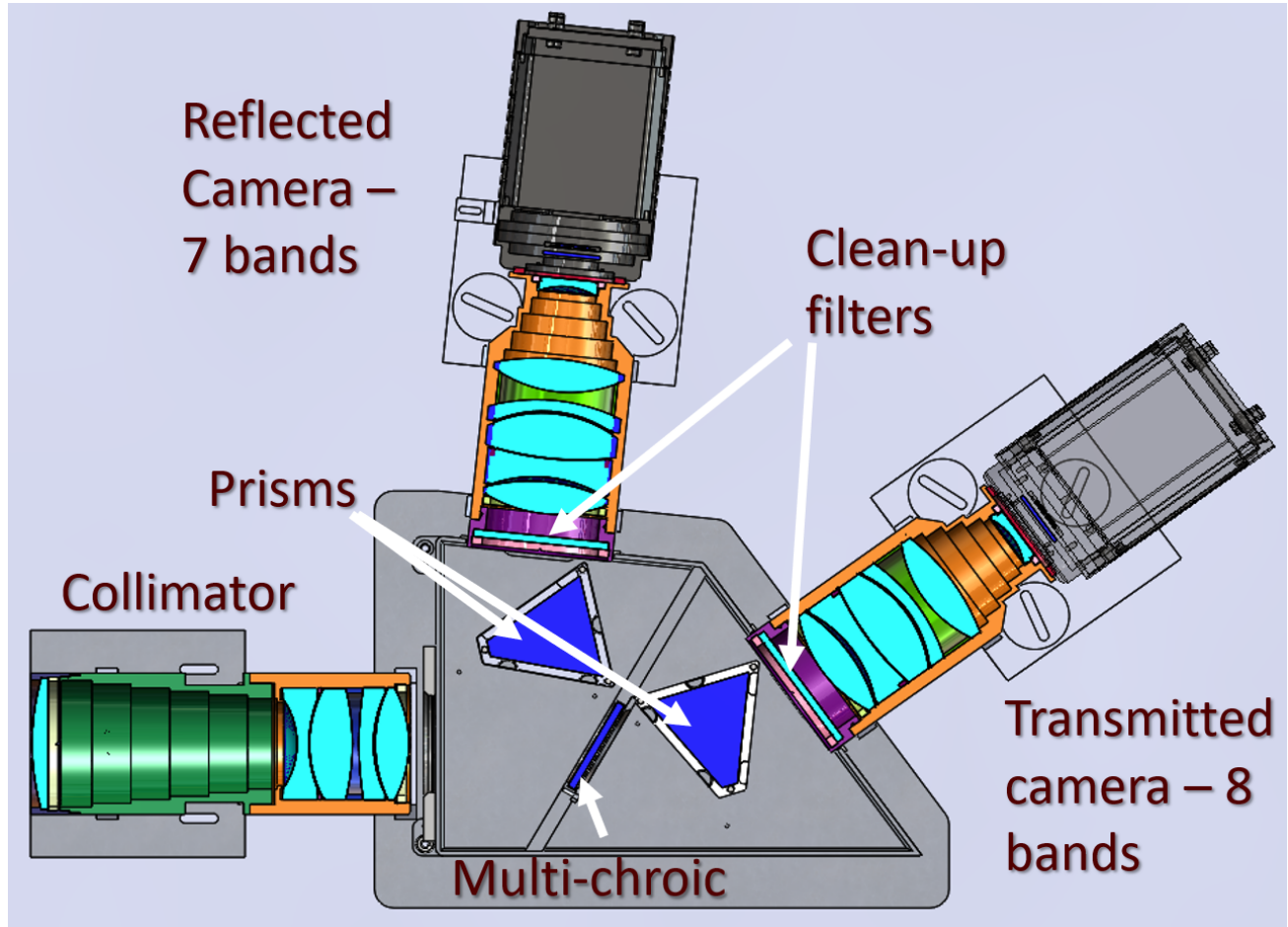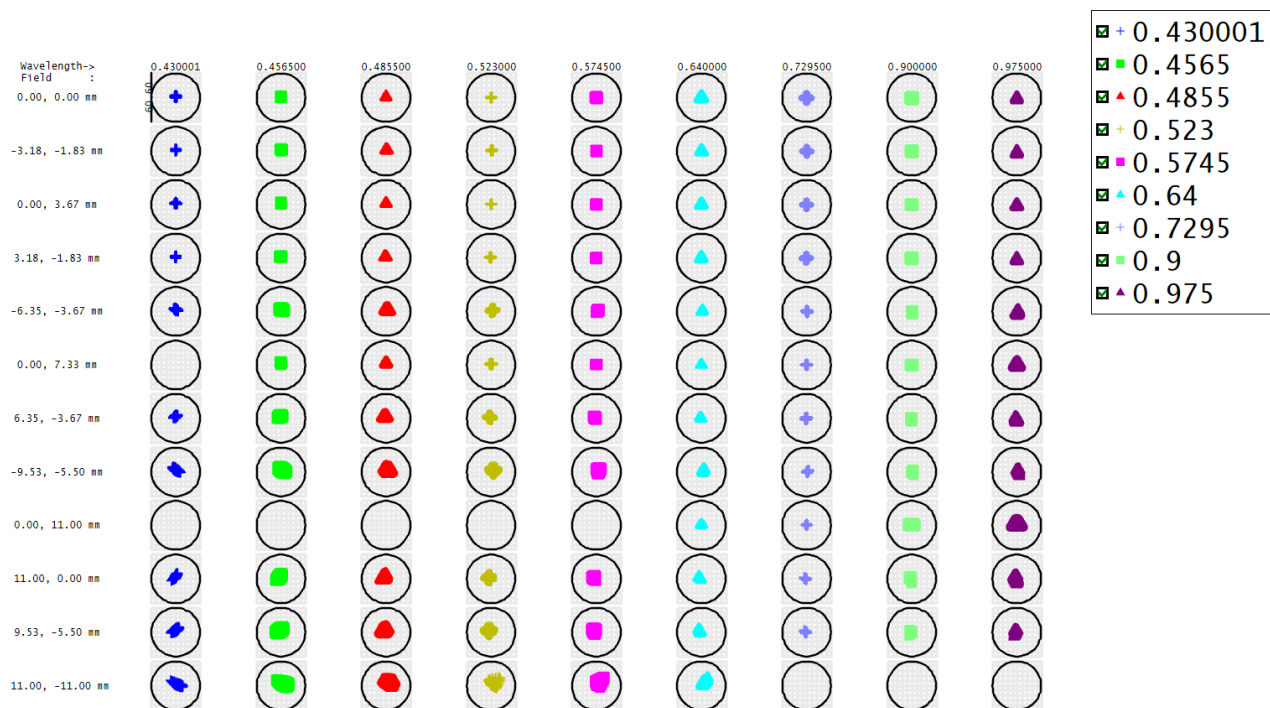Additional considerations for each optical assembly are in the following sections.

Figure 4: Section view of the ETSI optics and detectors. The telescope focal plane is to the left of the image. Light enters the collimator and is split into two channels by the multi-chroic which is located at the pupil. Identical prisms disperse the light which is then further filtered to sharpen the transmission cut on/off transitions and imaged with identical cameras onto sCMOS detectors.

3.1 Collimator & Cameras

ETSI has a five element collimator and identical six element cameras shown in Figure 4. The collimator is a reverse telephoto with the five lenses separated into three groups. Much of the design effort was focused on extending the distance from the last element of the collimator to the pupil. This was required to accommodate the 30° angle of the multi-chroic to ensure there was mechanical space for the prism in the reflected channel and that the collimator and camera lens barrels would have adequate clearance as well as space for a shutter to facilitate capturing calibration frames.

The six element cameras are split into three groups, with the final element being a field flattener. The camera optimization was constrained by the requirements listed above, as well as the required mechanical spacing between the pupil and front lens to accommodate the prisms and clean-up filters.

All lens elements for both collimator and cameras are air-spaced with spherical surfaces. After initially optimizing the camera and collimator separately, the majority of the optimization was as a complete system in order to optimize the collimator-prism-camera angles as well as optimize the prisms to achieve the desired spacing between filter bands.

Figure 5: Matrix spot diagram of ETSI and a paraxial McDonald Observatory 2.1 m telescope. The circles are 1 arcsecond in diameter. The field positions with missing spots are at the edge of the field and those wavelengths fall off the edge of the detector.

Final optimization of the optical design involved extensive discussion with the optical manufacturer (JML Optical) about blank availability and constraints on lens sizes as well as optimization of glass choices for a minimum of axial color. Of particular use was a technique where all air and glass thicknesses and surface radii were held fixed and only glass substitution was enabled for a limited catalog of glass types, based on vendor availability with some exclusions due to cost or manufacturing concerns. The previous merit function weights are almost entirely set to zero, with only constraints on the focal length and axial color by minimizing the rms change in focal length at each of the ETSI filter bands.[23]

In combination with the McDonald Observatory 2.1 m telescope, ETSI has an overall focal ratio of $f/6$, which results in a plate scale of 0.18"$/px$ and a 6.2$'$ field of view.

Table 1: Collimator and cameras as built optical performance. Requirement was on-axis 80% encircled energy within a 25.4μm spot size for the collimator and on-axis 80% encircled energy within a 12.7μm spot size for the cameras, tested at three wavelengths.

Filter	Field Position	Collimator EE80 (μm)	Camera 1 EE80 (μm)	Camera 2 EE80 (μm)
440 nm	on axis	5.2	7.6	4.2
632 nm	on axis	11.5	5.1	9.4
900 nm	on axis	7.6	6.0	7.9

3.2 Filters

The key optical components that makes ETSI possible are the multi-chroic and clean-up filters in each channel. These filters are thin film optical interference filters with many alternating layers of high and low index dielectric materials. Filters are generally deposited using Physical Vapor Deposition (PVD) in vacuum chambers and layers are controlled to within a few nanometers of physical thickness. A complete description of the filters and the filter design process is given in Limbach et al.[24] The multi-chroic is located at the pupil and is responsible for the inital splitting of the light into eight transmitted bands and seven reflected bands. The 30° angle of the multi-chroic and the out of band blocking (OD3 req. OD4 goal) and transmission to reflection transition zones made it difficult to meet specifications with only a single optic.

The filter bands were chosen to coincide with exoplanet atmospheric features. We modeled dozens of exoplanet atmospheres using Exo-Transmit[25] and aligned the spectral bands with detectable molecular and atomic absorption features. Two small portions of the spectrum (680-697 nm and 797-847 nm) are blocked completely in order to maintain adequate spacing between spectral bands of interest on the detectors. To transmit only the desired bands to each camera, additional clean-up filters are added after the prisms. Figure 6 and 7 show the individual and combined transmission of the ETSI optical components, separated into reflected and transmitted bands.

3.3 Prisms

In order to perform photometry on each individual band, N-SF5 prisms disperse the light, separating the filter bands into distinct PSF's which results in the unique dashed-line appearance of ETSI images (see Figure 17. The optical face of each prism is 75 mm on a side with a prism angle of 46.24°. A complete discussion of the prism design process is described in Limbach et al.[24] Attempts were made to develop a zero deviation prism design, but were ultimately discarded due to the number of prisms and materials required and space constraints. The blue bands are slightly over dispersed and produce a lower signal-to-noise (SNR) ratio, especially on cooler stars. However, multiple bands in the blue portion of the spectrum can be combined in post processing where the SNR is insufficient to provide useful exoplanet atmospheric constraints. Gratings were not considered due to scattered light concerns, very low groove densities, and lower transmission when compared to prisms. Note that high instrument transmission is extremely important for exoplanet transmission spectroscopy as measurements are limited by photon noise of the host star. The final prism angle and position relative to the collimator and cameras was included in the overall optical design optimization. To further minimize stray and scattered light, the non-optical surfaces of each prism were blackend with Speedball Super Black India Ink, chosen for its low reflectivity across the full optical spectrum and ease of application.[26] Figure 8 shows the dramatic difference in appearance that results from this process.

4. OPTOMECHANICAL DESIGN

The optomechanical concept mimics a typical experimental setup in a laboratory, with an optical bench that all optics are mounted to with the optical axis 4" above the bench surface. The optical bench is then supported by a frame, with panels to seal the instrument from stray light and dust. This layout was chosen to provide maximum flexibility. It was uncertain if an additional guide camera would be required, or if guiding could be done from the science images, so extra space was left in the enclosure. This also allows for flexibility to choose different filters
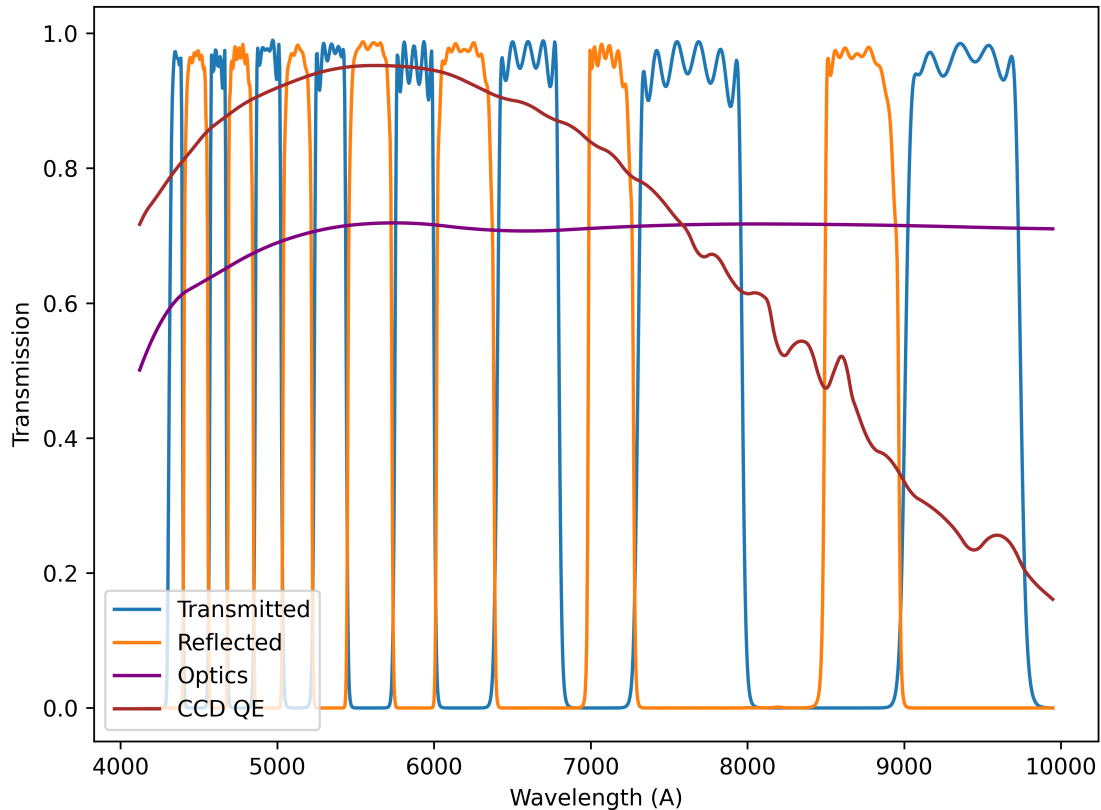
Figure 6: Transmission of the various ETSI optical components as reported by the vendors. Transmitted and reflected filters, optics includes the collimator, camera and prisms.

and prisms without requiring a complete redesign of the support structure. The following subsections describe each part in greater detail.

4.1 Optical Bench and Support Structure

The optical bench is a lightweight composite assembly to minimize both weight and changes with temperature. Manufactured by Vere Inc., the total bench mass is 28.6 kg and is $1.0 \times 1.15 \times 0.112\ m$. The top side of the bench has a grid of M6 threaded holes on a 25 mm spacing. The bottom of the bench has 3×3 equally spaced patterns of four M6 threaded holes in a square pattern, 50 mm on a side. This enables easy mounting to the support structure when mounted to the telescope, or to the top of a large laboratory optical table during alignment and testing.

A lightweight carbon fiber frame, constructed using a modular system from Dragonplate[*], was designed. This system uses preformed carbon fiber tubes and gussets which are bonded together with Scotch-Weld 2216 adhesive which is held together during the curing process with pop-rivets. The tubes are easily cut to length using a standard tile cutting wet saw to minimize carbon fiber dust.

The telescope facing side of the 2" square tubular frame would be bonded to an interface plate made from a CNC cut sheet of 1" thick structural foam core sheet material with a Divinycell H100 core and three layers of

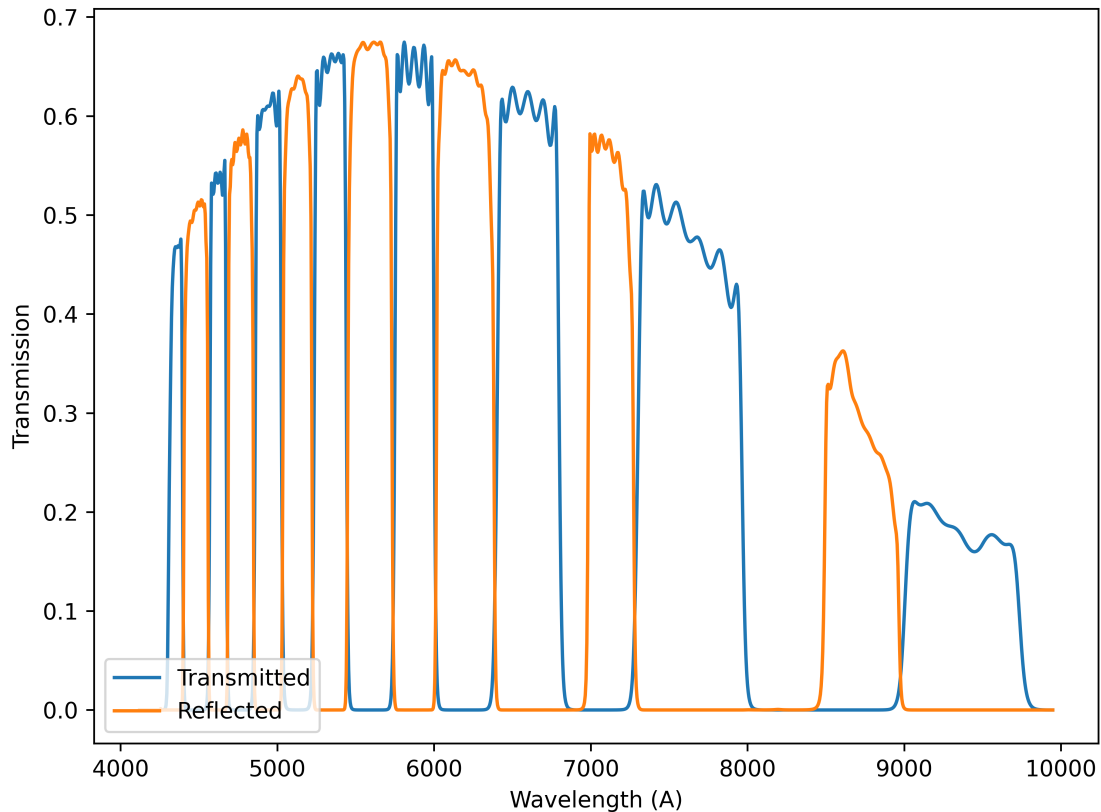---

[*]https://www.dragonplate.com

Figure 7: The efficiency of both channels including collimator, multi-chroic, prisms, clean up filters, camera optics, and detector quantum efficiency.

plain weave carbon fiber bonded to each side. Stainless steel adhesive mounted nuts are bonded to the back side of the foam core sheet to allow a 1/2" thick Aluminum tool plate to bolt to the foam core sheet (see Figure 9a. This dual plate configuration enables a good bonding interface to the carbon fiber frame, while still providing a robust Aluminum interface to the telescope, which is better suited to frequent mounting [removal] to [from] the telescope.

ETSI is mounted to the telescope via an Aluminum spacer constructed from a 6" long, 1/2" wall thickness tube and 1/2" tool plate telescope interface ring (six 1/2"-13 bolts on 13.625" B.C.). The other end of the tube bolts to the 1/2" thick Aluminum front plate.

The sides are covered with 3 mm thick Dibond Aluminum skinned plastic composite panels, sealed with a thin foam gasket and held on to the structure with captured hardware (Southco TL-05-100-52 slide latches).

Ventilation is provided by 4" circular "dark room" vents that allow airflow without a direct path for stray light to enter. Internal air exchange is enhanced by low voltage fans at two vent locations. Dust and water tight cable grommets are used for control cables. Power supplies for cameras and other electronics are mounted to the the outside of the enclosure.

The connection between the support frame and optical bench is a 3-2-1 constraint configuration. Three ball ended adjustment screws and a cone block and two vee-blocks connect the optical bench to the frame. Once
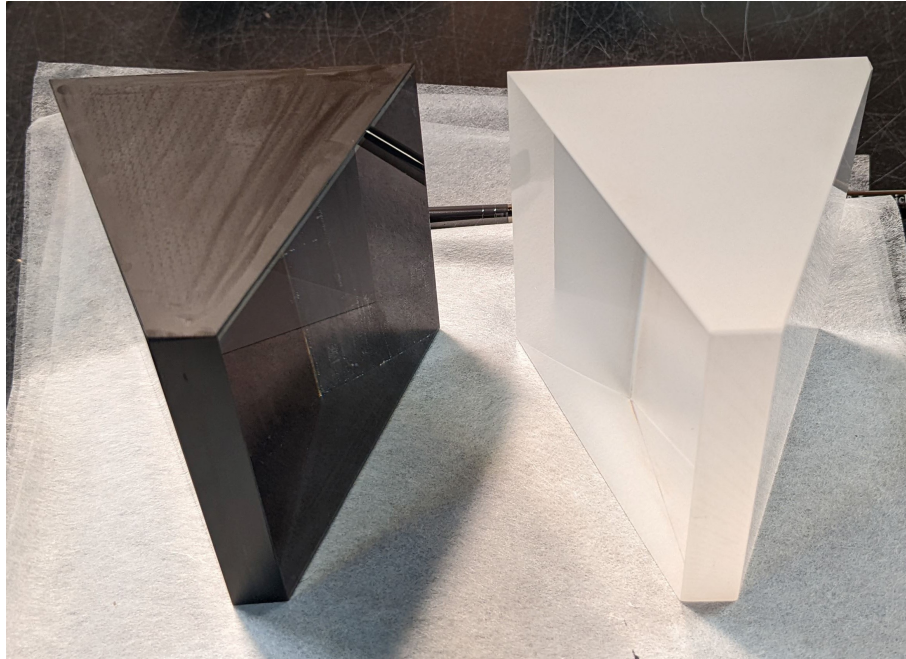
Figure 8: The ETSI prisms, the left prism has had the non-optical surfaces painted with India Ink to reduce scattered light.

(a)

Load spreader, connected to underside of optical bench

Steel insert ("cone")

Spherical end adjustment screw

Frame mount with threaded insert

Locking nut
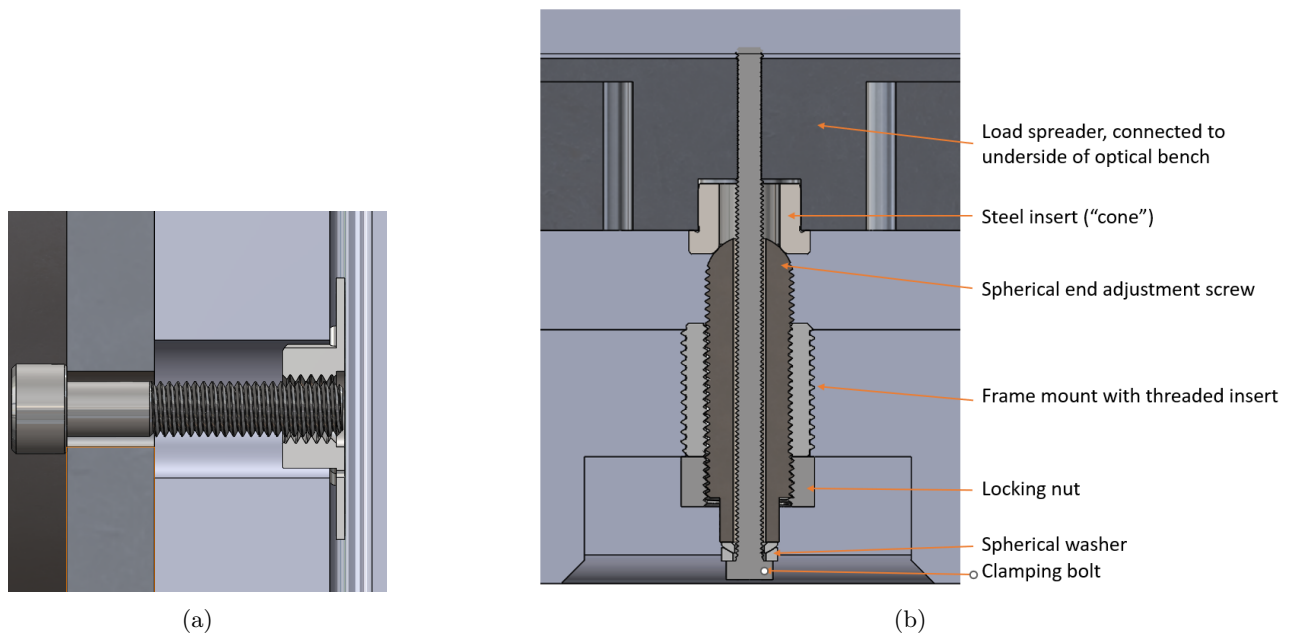
Spherical washer

Clamping bolt

(b)

Figure 9: a: Section view showing the structural foam plate sandwiched between the Aluminum front plate and adhesive mount nut. b: Section view showing one of the adjustment and mounting points between the support frame and optical bench.

adjusted, they can be locked in position with a locking nut, spherical washers and slightly oversized holes allow for small tilts between the clamping bolt and adjustment bolt (see Figure 9b). Further constraint against rotation is accomplished via three ball joint turnbuckle assemblies that are a fixed length, but allow movement in the other degrees of freedom so as to not overconstrain the assembly.
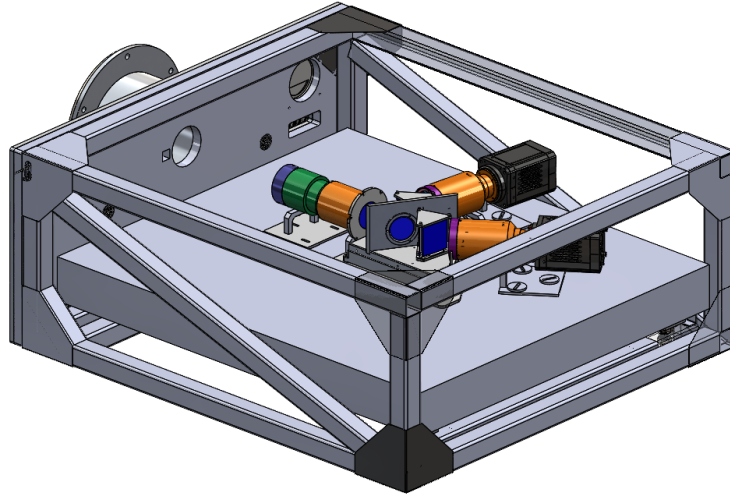
Figure 10: The modular carbon fiber frame is shown with the optical bench and optics mounted.

Figure 11: Temporary extruded frame with two of the side panels attached. A removable cart (silver extrusions) allows ETSI to be rolled around the lab, or into position when mounting to the telescope.

The use of lightweight/composite materials was selected to minimize instrument flexure as well as any potential thermal changes over the course of a typical transit observation (~4-6 hours). However, supply chain issues and other delays required construction of an alternate support frame (Figure 11) from extruded Aluminum structural T-slot frame and fittings in order to be ready for the commissioning run allocated telescope time. The optical bench was rigidly supported at three points with flat aluminum plates between the bottom of the optical bench and the T-slot frame. Removable covers were constructed from corrugated plastic panels. This support frame has performed admirably during commissioning and initial science observations. Weather patterns were relatively stable and only small temperature changes were seen each night (~ 3°C). We expect to complete the carbon fiber frame for future observing runs, which should have improved stability during larger temperature swings.

Figure 12: Bottom view of one of the camera barrels showing the locations of the hole and slot to receive the pins in the mounting bracket with threaded holes for the m4 screws to secure the barrels to the mounts.

4.2 Optical Mounts

The collimator and cameras were purchased as complete optomechanical assemblies. The design of the mounting interface between the lens barrels and supports as well as to the detectors was a cooperative effort with the vendor. The detectors are mounted with four M3 screws from the camera barrel flange to the body of the detector. The back focal spacing is set by a captured ring, machined to the correct thickness. The focus between channels is matched by placing a pinhole at the location of the telescope focal plane, illuminated by an integrating sphere. The pinhole location is adjusted so that the transmitted camera is in focus with a spacer set for the nominal back focal distance. The reflected channel is then focused to match by adjusting the spacer between the camera barrel and detector. Each lens barrel is supported by two U-shaped aluminum pieces, mounted to plates that are screwed to the optical bench. Each lens barrel support has a 3mm pin in the center, with captured m4 screws on either side. The lens barrels have matching holes for the pin and threaded holes for screws on one end, and a slot with threaded holes for the screws on the other end (Figure 12). This enables positioning and alignment in the lab by adjusting the mounting plate on the optical bench, then the lens barrels can be removed for transport to the observatory and repeatably mounted upon arrival at the telescope. It practice this has worked wonderfully, during the two times ETSI has been assembled at McDonald Observatory, the optics and cameras have been mounted to the breadboard with no additional alignment in only a few minutes. The detectors remain mounted to the lens barrels for transport.

One support of each lens barrel is mounted to a central locating plate. This sets the correct position of all lens barrels relative to the multi-chroic and prisms. The other end of each barrel is on its own plate which allows slight repositioning for fine adjustment of the alignment. In practice the alignment tolerances between collimator, multi-chroic, prism, and camera barrel are loose enough that the assembly can be attached to the bench using only the grid of M6 threaded holes for reference. Alignment was checked using a Faro coordinate measuring arm and each lens barrel was within ~ 8 arcmin of the optical axis. This level of misalignment was undetectable in lab images and negligible when modeled with Zemax. The self referencing technique used in the ETSI instrument removes most systematic errors that would typically arise due to misalignment or flexure, thus eliminating the need for extremely tight instrument tolerances.

The multi-chroic and prisms are mounted to an Aluminum support plate that was machined out of a single piece of tool plate (Figure 14). It has a slot to hold a plate at the 30° multi-chroic angle. The multi-chroic is mounted into this plate in a circular recess and held in place with a retaining ring with o-ring spacer.

The prisms are mounted in a 3-2-1 style fixture. They sit on three pads machined into the mounting plate to set the prism height and rotation along two axes and further constrained by two cylindrical contact points on
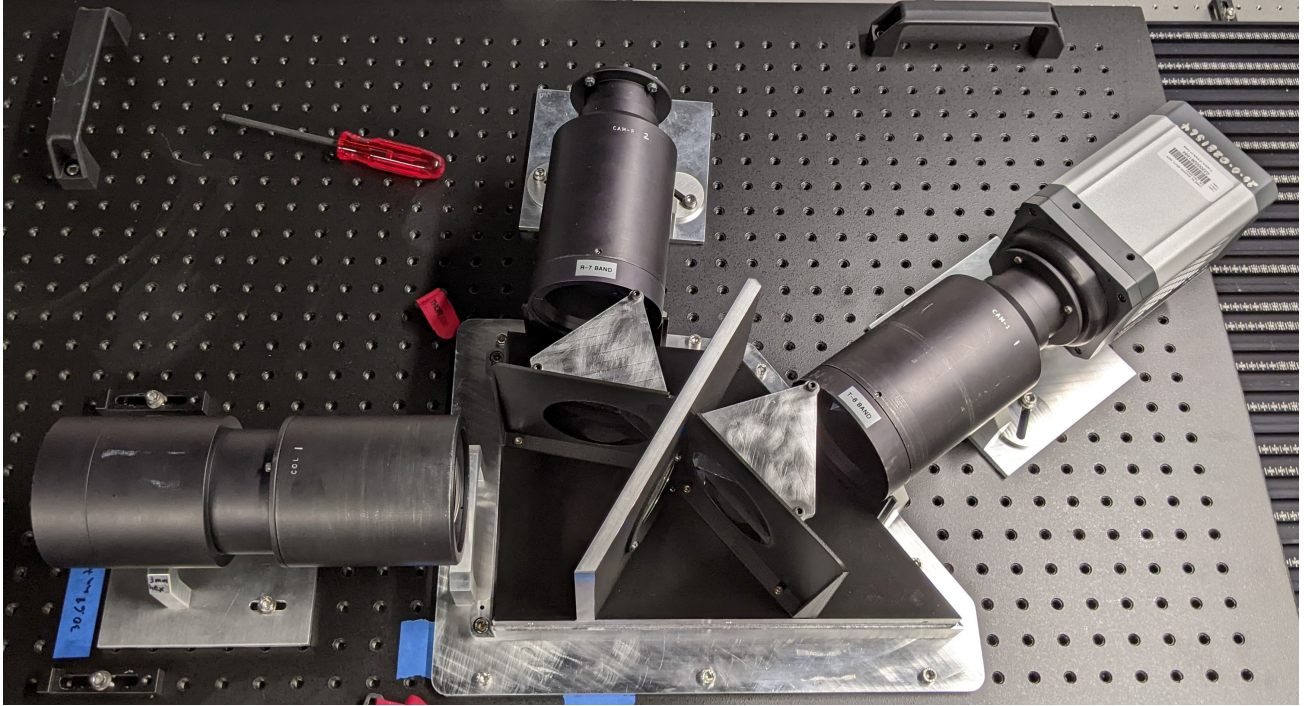
Figure 13: ETSI assembled in the lab for testing, the central locating plate with prisms and filter mount is in the center, support plates for the collimator and cameras are visible. The camera supports are held to the table with slotted disks that fit into oversize holes in the plate. This allows the disks to rotate and align the slot with one of the holes in the optical bench. Also visible are 3D printed baffles in front of the prisms to prevent any stray light from making its way around the sides of the prisms.

one face of the prism and one cylindrical contact point on a second face. An Aluminum plate clamps the prisms onto the prism base via three long screws, one at each corner. A thin textured rubber sheet is placed between the top of the prism and the clamping plate to allow for differential expansion and contraction due to temperature changes. Baffles were 3D printed and internal surfaces coated with light absorbing Fineshut SP urethane foam (see Paper 12188-177 in these proceedings for total reflectivity measurements of this material), see also Figure 13. The prism and multi-chroic mount assembly is covered with a 3D printed cover. The entire assembly can be removed from the locating plate by removing three M6 screws. Position repeatability is achieved by pins and a hole and slot near two of the three mounting points (visible in Figure 14).

5. ELECTRONICS & SOFTWARE

5.1 Detectors

The recent availability of high quality optical CMOS sensors (often referred to as sCMOS or scientific CMOS) has proven crucial to the success of ETSI. An early prototype used a commercially available CCD. There were no issues with the data quality, however even at the highest read out speed the observing efficiency was very low. In order to measure the small color changes during a transit, averaging over many measurements is required and the overall sensitivity is driven by the total number of photons detected. For bright targets especially, the exposure time can be shorter than the read out time of the CCD, resulting in many missed photons. Additionally, read noise becomes an issue at all but the slowest read out rates.

One possible solution considered was to switch to a frame transfer Electron Multiplying CCD (EMCCD). Frame transfer allows for faster read rates and the electron multiplication process can essentially eliminate read noise under certain observational conditions, however for any pixels where the shot noise is above the readout noise, the signal to noise ratio is reduced by a factor of $\sqrt{2}$ due to the stochastic nature of the electron
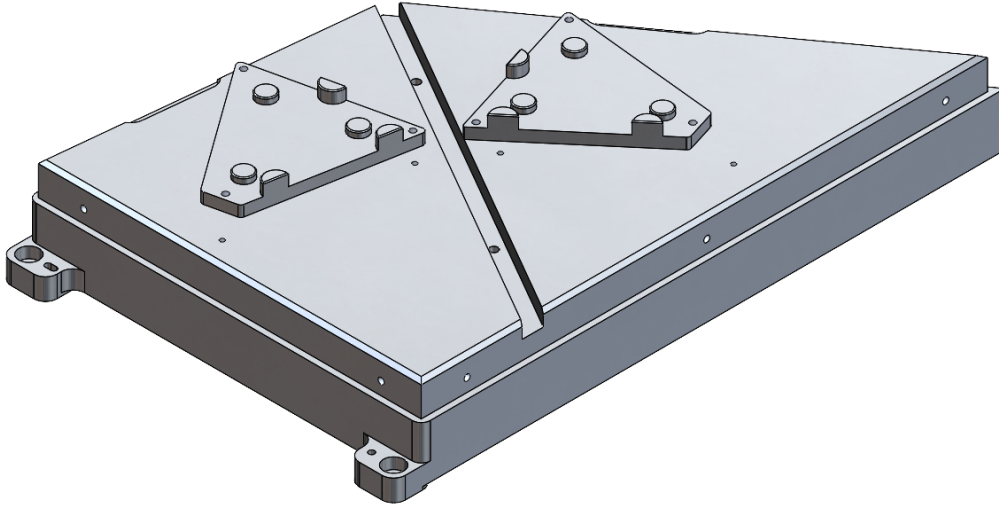
Figure 14: The prism base. A slot for the multi-chroic mount is visible with machined prism locating points on either side. This piece was machined out of a single piece of 2.5" thick tool plate, the underside has been light-weighted to a 5mm wall thickness.

multiplication process. Effectively this means that EMCCD's are best suited for low photon counts. The electron multiplication process also effectively reduces the possible dynamic range, so a 16-bit EMCCD has an equivalent, or even lower dynamic range than the 12-bit readout of an sCMOS detector for higher EMCCD gain values.

The latest generation of sCMOS devices solve essentially all of these issues, with future generations promising even better performance. Our chosen detector, the Andor Marana sCMOS camera is based around the GSENSE400BSI sensor a back illuminated, $11\mu m$ pixel, $2048 \times 2048\ px$ array. The large pixel size and high quantum efficiency (peak QE of 95%) make for efficient collection of photons and the readout time of $\sim 20\ ms$ enables a minimum of observation time lost to readout. Read noise is $< 2e^-$ at all frame rates. One aspect of the current generation of sensors we are still evaluating is the inclusion of a dual amplifier architecture, where each pixel is read by two amplifiers, each with a different gain. Two readout modes are available, either a "high gain" mode, in which a single amplifier is used and the output is a 12-bit image, or a "high dynamic range" mode where on a pixel by pixel basis a decision is made on which amplifier to use (if the high gain amplifier is saturated, the low gain amplifier is used). The two data streams (high and low gain) are digitized at 12-bits and are then set to a common linear scale and converted to 16-bits. We are collecting data on standard stars for all readout modes to evaluate any potential systematic errors. Currently we are collecting any transit data in the "high gain", 12-bit output mode. This can result in higher data rates (~ 10 frames per second for an 8th magnitude star on the McDonald 2.1 m telescope) to avoid saturation, but was decided to be the conservative approach until a full analysis can be performed on the dual-readout 16-bit data.

5.2 Communication, Temperature Monitoring, & Shutter

ETSI has essentially no moving parts with the exception of a Uniblitz NS65B bi-stable optical shutter controlled with a Uniblitz VED24 shutter driver. The shutter is located betwen the collimator and multi-chroic to allow for acquisition of dark and bias calibration frames and is mounted to the entrance port of the 3D printed prism and multi-chroic mount cover. It is not used during normal observations due to the high frame rates (the rated continuous operation frequency is 1Hz). Instrument internal and external temperatures are monitored via low cost 1-wire DS18B20 temperature probes. All control and interface signals are via USB. Two operational modes have been used, the default mode is a FireNEX-5000Plus USB 3.1 fiber optic extender, which has a four port hub on the remote unit and is then connected to a local unit via duplex single mode fiber. This allows the control computer to be located in the control room. The most recent observation run required mounting the control

computer inside the instrument enclosure and controled via remote desktop due to a broken fiber optic. Both operational configurations worked and we are evaluating the benefits of each for long term operations.

5.3 Camera Control

The Andor Marana sCMOS camera is controlled by a Python program that uses the Andor SDK and andor3 Python interface.[27] The andor3 Python interface includes utilities that control the frame buffer and frame delivery to the rest of the program. A user interface allows observers to set up each acquisition sequence. Settings such as exposure time, co-add count, and gain (12-bit or 16-bit) are selected by the user and sent to the camera. When the camera is commanded to begin taking frames, the frame buffer waits for each new frame and delivers the frame to a callback function. The callback function saves each frame as a FITS file with informational headers that include position, environmental, and tracking information from the McDonald Observatory 2.1 m telescope control system.

5.4 Interface with McDonald Observatory 2.1 m telescope TCS

The position and tracking information from the McDonald Observatory 2.1 m telescope control system (TCS) is collected by connecting to the TCS network and requesting the information once every second. Between each request, the information is stored so it can be inserted into each frame's FITS header as each frame arrives. Additionally, a frame or stack of frames is sent to the 2.1 m auto-guiding software Guide82 every 10 seconds. Guide82 also reports estimated fwhm of the images and includes an automated focusing routine.

6. THE ETSI DATA REDUCTION PIPELINES

6.1 The ETSI Quick Look Pipeline

The ETSI Quick Look Pipeline (QLP) provides real-time analysis of target photometry concurrent with ETSI observations while users are at the telescope. This graphical user interface tool is meant to provide users with real time estimates of both the white light curve of the target star and a user selected color. The pipeline executes via an IDE interface where users update a configuration file with the star's name, exposure time, and a location to output the real-time figure.

The QLP runs independent of camera acquisition and will wait for images if they are not currently available for reduction. Once a first image is found, a screen displays where users select the location of the target star and one or more companion stars, if available. By default the QLP uses the first image in the sequence as the reference image, but users are capable of selecting a different image for reference should the first image be unacceptable due to clouds, satellites, or other obstructions. After the location of all stars have been selected, users select the two ETSI bandpasses in order to generate a color for real time comparison during observation. This procedure is executed for both transmission images and reflection images. After users have selected the PSF on the reference image, the QLP is independent for the remainder of observations.

The QLP automatically registers each new image to the reference image using `astroalign`, finds the updated centroids for each PSF, and extracts the flux for each PSF using a fixed-sized 35×15 pixel elliptical aperture with the `PYTHON` implementation `photutils`.[28,29] The flux from each individual PSF is then summed together to generate a synthetic "white-light" flux for each star which is then converted to an instrumental magnitude. A zeropoint offset is calculated between the reference frame and the current frame using the median offset between each comparison star's magnitude in the current frame and the magnitude of the star in the reference frame. This offset is then subtracted from the target star's magnitude. The star's color change is calculated by subtracting the instrumental magnitude of the two previously selected target star bandpasses. These corrected magnitudes, as well as the image's time stamp, are output to a text file.

After every subsequent 5 minutes of exposure time have been reduced, the output data is read from the text file, binned into 5 minute intervals, and plotted to show the white light curve and the estimated color change. Additionally, a linear fit to the color change is plotted on the figure for estimation purposes. A representative QLP figure is shown in Figure 15.
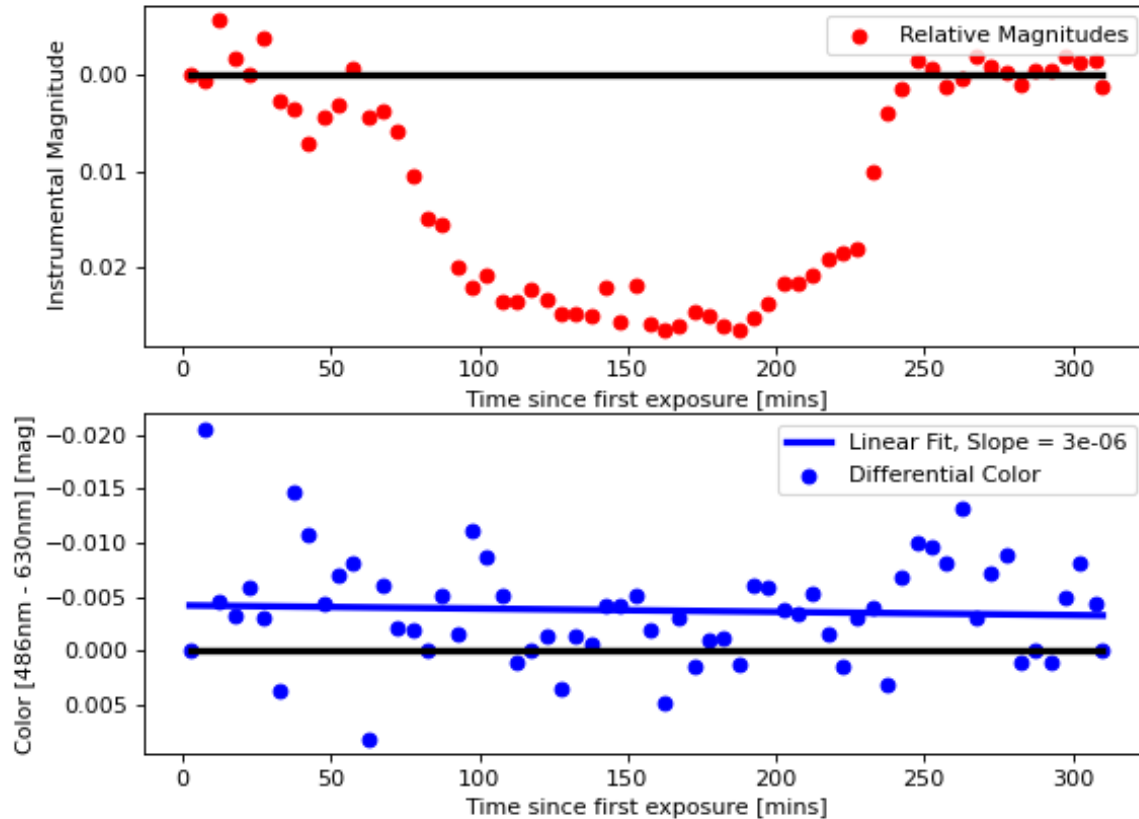
Figure 15: An example of a real time light curve output by the QLP for transmission data taken during the April 2022 commissioning run. The top panel shows the white light curve generated by summing the flux in all tranmission bandpasses of a transitting exoplanet. The bottom panel shows the relative color offset between two ETSI colors with a simple linear fit to the color change. These figures are meant to be representative outputs of the QLP and do not necessarily display accurate color changes.

6.2 The ETSI Data Reduction Pipeline

The full data reduction suite for ETSI consists of three main components: image calibration, photometry extraction, and systematics removal. ETSI images are calibrated using a bias subtraction and a residual sky subtraction. The data is not flat-fielded as we have found flat fielding to increase the uncertainty in the final photometric measurements. A master bias frame is generated through a median combination of 200 single bias frames taken before and after the observations. Next, a residual background subtraction is constructed to remove large-scale structure from clouds or scattered light.[30–32] The residual background model is constructed by sampling the sky background every 128×128 pixels over the entire detector. Bad or saturated pixels are excluded from each sky sample and replaced with the median sky value in the 128×128 pixel box. A model sky is then fit inside each box and interpolated between all boxes using the PYTHON implementation griddata to make a thin plate spline[33] which is subtracted from each frame.

Photometry is extracted from each image using both fixed-size aperture photometry and point-spread-function (PSF) photometery. A master image is used to locate the position of each spectral PSF and to generate a model PSF to use for photometry. Each cleaned image is registered to the orientation of the first image using

`astroalign`, and then these aligned images are median-combined to generate the master image.[28] The locations of the target and comparison stars are manually selected and centroided on each master frame to provide an initial estimate for the positions of each PSF. This manual selection of the PSF locations is preferred over an automatic selection given the varying SNR values of each PSF and the unique ETSI PSF shape which was shown to create issues for most automated detection software. The ESTI PSF is then extracted from the master frame using the `PYTHON` photometric software `photutils`.[29] Each of these manually selected positions is re-centroided on every science image and stellar flux is extracted using a fixed-size elliptical aperture of 40×25 pixels, and the previously mentioned ETSI-specific PSF. Initial tests of the photometric quality suggest the PSF-photometry provides light curve dispersion equal-to or smaller than the fixed-aperture photometry by $\sim 50\%$.

Finally, possible detector systematics are removed from the photometry using a nearby comparison star when available. Systematics can vary between observations and the number of available comparison stars can change the quality of the final light curves. Therefore, we have been testing several methods which may be implemented in the final version of the data reduction pipeline. These methods include:

- Comparison star detrending: Typically, two stars of similar magnitude should not vary in identical astrophysical patterns between images, even if they were the same spectral type or variable type. In many cases, the bandpass specific flux from a comparison star can be binned using a moving mean and used to normalize the target star's bandpass flux and remove common systematics.[30,32,34]

- Self-referential detrending: This method would typically be used in the event no comparison star of similar magnitude is available. The ETSI science goals are only interested in referential measurements, not absolute measurements. Therefore, a trend can be generated through a median combination of all of the target star's bandpass light curves, re-scaled, and then subtracted from each individual bandpass light curve. Figure 16 shows an example light curve for HD 94833 after using this method.

- Observational Bias detrending: Ground-based observations will suffer from changes due to airmass, extinction from clouds, changes in the temperature of the detector, and the slight changes of the position of the star on the detector. A trend could be generated through a linear or polynomial combination of these factors to remove systematics which are not found to be correlated between the target star and its comparison.

Light curves have been investigated for several objects using data obtained by the instrument during April 2022 commissioning. One such object, HD 94883, is an A2 star observed at a cadence of 0.2 s over a baseline of ~ 1.5 hours. The change in magnitude for each bandpass was found to be consistent with a flat line ($R^2 \sim 0$), and the mean change in color of HD 94883 was found to be 0.05% over 90 minutes of observations.

7. COMMISSIONING

ETSI had first light April 19-24, 2022 on the McDonald Observatory 2.1 m telescope with only the transmitted channel, allowing simultaneous photometry of eight spectral bands. Additional commissioning and science observations occurred June 6-21, 2022 and July 6-19, 2022 also on the McDonald Observatory 2.1 m telescope with both transmitted and reflected channels.

7.1 Preliminary Results

Light curves have been investigated for several objects using data obtained by the instrument during April 2022 commissioning. One such object, HD 94883 shown in Figure 16, is an A2 star observed at a cadence of 0.2 s over a baseline of ~ 1.5 hours. The change in magnitude for each bandpass was found to be consistent with a flat line ($R^2 \sim 0$), and the mean change in color of HD 94883 was found to be 0.05% over 90 minutes of observations. We expect this precision to improve as data reduction methods are optimized.
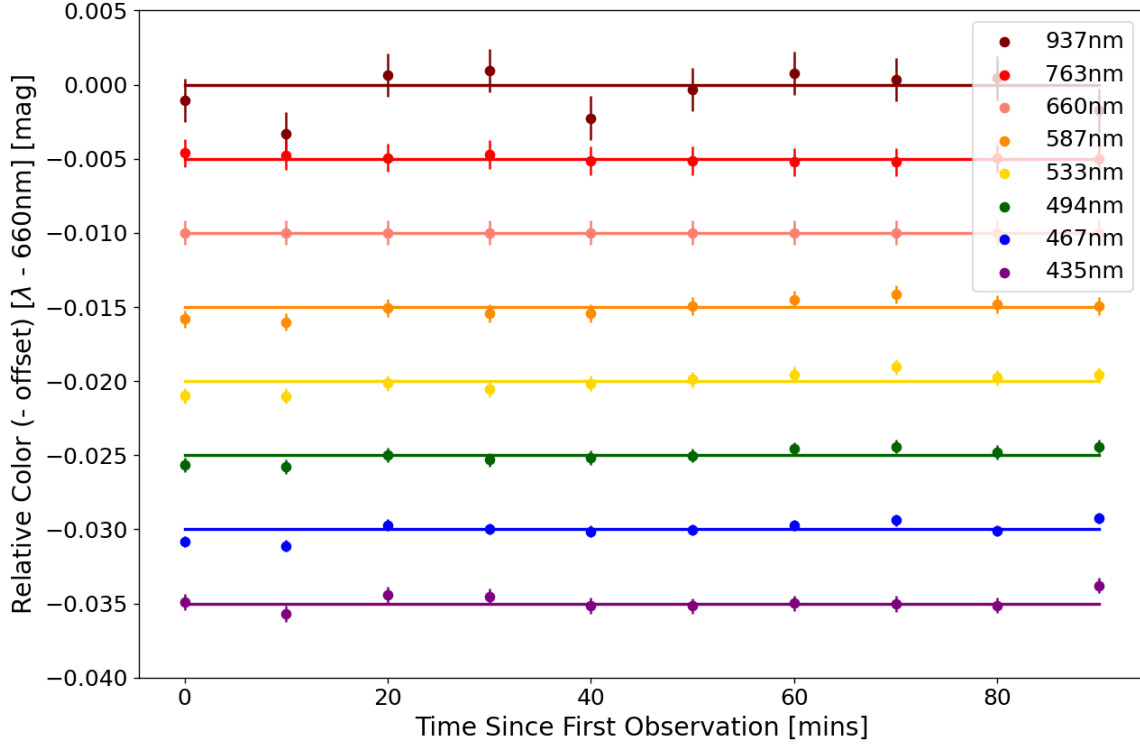
Figure 16: Eight representative light curves of the color change of HD 94883 (an A2 star) over the course of 90 minutes using ETSI observations from the April 2022 commissioning run. The relative color was calculated by subtracting the 640 nm bandpass from each other bandpass. The data has been binned into 10 minute intervals and each color is offset by 5 mmag for clarity. The uncertainties shown have been scaled to match the dispersion in the data. The solid lines assume no change in color and are not a fit to the data. The change in color over the course of the 90 minute observations was found to be consistent with a flat line ($R^2 \sim 0$) for all bandpasses, and the mean change in color of HD 94883 was found to be $\sim 0.05\%$ over the 90 minutes of observations.
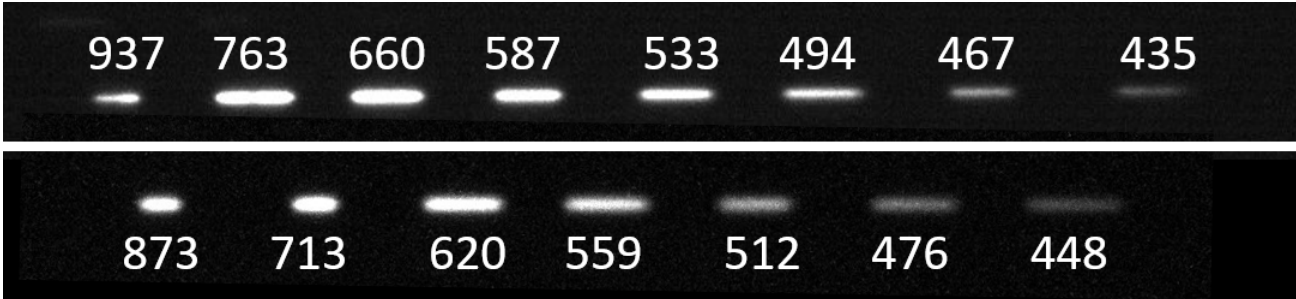

Figure 17: Images of an F-type star showing the 8 bandpasses from the transmitted channel (top) and 7 bandpasses from the reflected channel (bottom), offset to show that when combined, ETSI captures almost complete wavelength coverage from 430-975 nm. Bands are red to blue, left to right. Central wavelength is given in nm above/below each band.

8. CONCLUSIONS

ETSI is a unique instrument that leverages the advantages of simultaneous multi-bandpass photometry and is made possible by several key technologies, including multiband interference filters and sCMOS detectors. Early results are promising and indicate ETSI will be a highly productive instrument, characterizing exoplanet atmospheres in only a few transits. We are actively exploring ETSI's applicability to other science targets such as supernovae, variable stars, and rapid characterization of other transient events. ETSI has four science runs (a total of 50 nights) between June and October of 2022 and is expected to obtain transmission spectra of about a

dozen exoplanets during these observations. Work is ongoing to determine the most appropriate data reduction techniques for the unique multi-band images generated by ETSI.

ACKNOWLEDGMENTS

REFERENCES

[1] Walraven, T. and Walraven, J. H., "A new photoelectric method of classification of luminosity and spectral type for O and B type stars.," *Bulletin of the Astronomical Institutes of the Netherlands* **15**, 67–83 (July 1960).

[2] Florentin Nielsen, R., Nørregaard, P., and Olsen, E. H., "First fully automatic telescope on La Silla.," *The Messenger* **50**, 45–46 (Dec. 1987).

[3] Mislis, D., Mancini, L., Tregloan-Reed, J., Ciceri, S., Southworth, J., D'Ago, G., Bruni, I., Başturk, O., Alsubai, K. A., Bachelet, E., Bramich, D. M., Henning, T., Hinse, T. C., Iannella, A. L., Parley, N., and Schroeder, T., "High-precision multiband time series photometry of exoplanets Qatar-1b and TrES-5b," *Monthly Notices of the Royal Astronomical Society* **448**, 2617–2623 (03 2015).

[4] Narita, N., Fukui, A., Kusakabe, N., Watanabe, N., Palle, E., Parviainen, H., Montañés-Rodríguez, P., Murgas, F., Monelli, M., Aguiar, M., Prieto, J. A. P., Álex Oscoz, de Leon, J., Mori, M., Tamura, M., Yamamuro, T., Béjar, V. J. S., Crouzet, N., Hidalgo, D., Klagyivik, P., Luque, R., and Nishiumi, T., "MuS-CAT2: four-color simultaneous camera for the 1.52-m Telescopio Carlos Sánchez," *Journal of Astronomical Telescopes, Instruments, and Systems* **5**(1), 1 – 14 (2018).

[5] McElwain, M. W., Mandell, A., Woodgate, B., Spiegel, D. S., Madhusudhan, N., Amatucci, E., Blake, C., Budinoff, J., Burgasser, A., Burrows, A., Clampin, M., Conroy, C., Deming, L. D., Dunham, E., Foltz, R., Gong, Q., Knutson, H., Muench, T., Murray-Clay, R., Peabody, H., Rauscher, B., Rinehart, S., and Villanueva, G., "NIMBUS: the Near-infrared Multi-Band Ultraprecise Spectroimager for SOFIA," in [*Ground-based and Airborne Instrumentation for Astronomy IV*], McLean, I. S., Ramsay, S. K., and Takami, H., eds., **8446**, 2210 – 2223, International Society for Optics and Photonics, SPIE (2012).

[6] Christille, J. M., Bonomo, A. S., Borsa, F., Busonero, D., Calcidese, P., Claudi, R., Damasso, M., Giacobbe, P., Molinari, E., Pace, E., Riva, A., Sozzetti, A., Toso, G., and Tresoldi, D., "SIOUX project: a simultaneous multiband camera for exoplanet atmospheres studies," in [*Ground-based and Airborne Instrumentation for Astronomy VI*], Evans, C. J., Simard, L., and Takami, H., eds., **9908**, 1554 – 1568, International Society for Optics and Photonics, SPIE (2016).

[7] Limbach, M. A., DePoy, D. L., Schmidt, L. S., Barba, L., Glatzberg, A., Hudson, S., Marshall, J. L., and Ross, A. S., "Common-path multiband imaging (cmi): A new technique for measuring precision photometric colors," (in prep.).

[8] Stevenson, K. B., "A new method for studying exoplanet atmospheres using planetary infrared excess," *The Astrophysical Journal* **898**, L35 (Jul 2020).

[9] Ahrer, E., Wheatley, P. J., Kirk, J., Gandhi, S., King, G. W., and Louden, T., "Lrg-beasts: Sodium absorption and rayleigh scattering in the atmosphere of wasp-94a b using ntt/efosc2," *Monthly Notices of the Royal Astronomical Society* **510**, 4857–4871 (Jan 2022).

[10] Cartier, K. M. S., Beatty, T. G., Zhao, M., Line, M., Ngo, H., Mawet, D., Stassun, K. G., Wright, J. T., Kreidberg, L., Fortney, J., and Knutson, H., "Near-infrared Emission Spectrum of WASP-103b Using Hubble Space Telescope/Wide Field Camera 3," *Astronomical Journal* **153**, 34 (Jan. 2017).

[11] Louden, T., Wheatley, P. J., Irwin, P. G. J., Kirk, J., and Skillen, I., "A precise optical transmission spectrum of the inflated exoplanet WASP-52b," *Monthly Notices of the Royal Astronomical Society* **470**, 742–754 (04 2017).

[12] Kirk, J., Rackham, B. V., MacDonald, R. J., López-Morales, M., Espinoza, N., Lendl, M., Wilson, J., Osip, D. J., Wheatley, P. J., Skillen, I., Apai, D., Bixel, A., Gibson, N. P., Jordán, A., Lewis, N. K., Louden, T., McGruder, C. D., Nikolov, N., Rodler, F., and Weaver, I. C., "ACCESS and LRG-BEASTS: A Precise New Optical Transmission Spectrum of the Ultrahot Jupiter WASP-103b," *Astronomical Journal* **162**, 34 (July 2021).

[13] Mollière, P., Wardenier, J. P., van Boekel, R., Henning, T., Molaverdikhani, K., and Snellen, I. A. G., "petitRADTRANS. A Python radiative transfer package for exoplanet characterization and retrieval," *Astronomy & Astrophysics* **627**, A67 (July 2019).

[14] Mollière, P., Stolker, T., Lacour, S., Otten, G. P. P. L., Shangguan, J., Charnay, B., Molyarova, T., Nowak, M., Henning, T., Marleau, G. D., Semenov, D. A., van Dishoeck, E., Eisenhauer, F., Garcia, P., Garcia Lopez, R., Girard, J. H., Greenbaum, A. Z., Hinkley, S., Kervella, P., Kreidberg, L., Maire, A. L., Nasedkin, E., Pueyo, L., Snellen, I. A. G., Vigan, A., Wang, J., de Zeeuw, P. T., and Zurlo, A., "Retrieving scattering clouds and disequilibrium chemistry in the atmosphere of HR 8799e," *Astronomy & Astrophysics* **640**, A131 (Aug. 2020).

[15] Foreman-Mackey, D., Hogg, D. W., Lang, D., and Goodman, J., "emcee: The mcmc hammer," *Publications of the Astronomical Society of the Pacific* **125**, 306–312 (Mar 2013).

[16] Kempton, E. M. R., Bean, J. L., and Parmentier, V., "An Observational Diagnostic for Distinguishing between Clouds and Haze in Hot Exoplanet Atmospheres," *Astrophysical Journal* **845**, L20 (Aug. 2017).

[17] Marley, M. S., Saumon, D., Visscher, C., Lupu, R., Freedman, R., Morley, C., Fortney, J. J., Seay, C., Smith, A. J. R. W., Teal, D. J., and Wang, R., "The Sonora Brown Dwarf Atmosphere and Evolution Models. I. Model Description and Application to Cloudless Atmospheres in Rainout Chemical Equilibrium," *Astrophysical Journal* **920**, 85 (Oct. 2021).

[18] Baraffe, I., Homeier, D., Allard, F., and Chabrier, G., "New evolutionary models for pre-main sequence and main sequence low-mass stars down to the hydrogen-burning limit," *Astronomy & Astrophysics* **577**, A42 (May 2015).

[19] Perryman, M., [*The Exoplanet Handbook*] (2018).

[20] Baraffe, I., Homeier, D., Allard, F., and Chabrier, G., "New evolutionary models for pre-main sequence and main sequence low-mass stars down to the hydrogen-burning limit," *Astronomy & Astrophysics* **577**, A42 (May 2015).

[21] Marley, M. S., Saumon, D., Visscher, C., Lupu, R., Freedman, R., Morley, C., Fortney, J. J., Seay, C., Smith, A. J. R. W., Teal, D. J., and Wang, R., "The Sonora Brown Dwarf Atmosphere and Evolution Models. I. Model Description and Application to Cloudless Atmospheres in Rainout Chemical Equilibrium," *Astrophysical Journal* **920**, 85 (Oct. 2021).

[22] Kurucz, R. L., "VizieR Online Data Catalog: Model Atmospheres (Kurucz, 1979)," *VizieR Online Data Catalog* , VI/39 (Oct. 1993).

[23] Siew, R., "Practical automated glass selection and the design of apochromats with large field of view," *Appl. Opt.* **55**, 9232–9236 (Nov 2016).

[24] Limbach, M. A., Schmidt, L. M., DePoy, D. L., Mason, J. C., Scobey, M., Brown, P., Taylor, C., and Marshall, J. L., "The Exoplanet Transmission Spectroscopy Imager (ETSI)," in [*Ground-based and Airborne Instrumentation for Astronomy VIII*], Evans, C. J., Bryant, J. J., and Motohara, K., eds., **11447**, 1634 – 1647, International Society for Optics and Photonics, SPIE (2020).

[25] Kempton, E. M. R., Lupu, R., Owusu-Asare, A., Slough, P., and Cale, B., "Exo-Transmit: An Open-Source Code for Calculating Transmission Spectra for Exoplanet Atmospheres of Varied Composition," *Publ. Astron. Soc. Pac.* **129**, 044402 (Apr. 2017).

[26] Schmidt, L. M., Aldoroty, L. N., Alam, Y., Bush, L., DePoy, D. L., Holden, M., Kim, D., Marshall, J. L., and Perkey, M., "Characterization of the reflectivity of various black and white materials," in [*Advances in Optical and Mechanical Technologies for Telescopes and Instrumentation IV*], Navarro, R. and Geyl, R., eds., **11451**, 575 – 581, International Society for Optics and Photonics, SPIE (2020).

[27] Tapping, P., "andor3, https://andor3.readthedocs.io/en/latest/," (Dec. 2021).

[28] Beroiz, M., Cabral, J., and Sanchez, B., "Astroalign: A python module for astronomical image registration," *Astronomy and Computing* **32**, 100384 (2020).

[29] Bradley, L., Sipőcz, B., Robitaille, T., Tollerud, E., Vinícius, Z., Deil, C., Barbary, K., Wilson, T. J., Busko, I., Günther, H. M., Cara, M., Conseil, S., Bostroem, A., Droettboom, M., Bray, E. M., Bratholm, L. A., Lim, P. L., Barentsen, G., Craig, M., Pascual, S., Perren, G., Greco, J., Donath, A., de Val-Borro, M., Kerzendorf, W., Bach, Y. P., Weaver, B. A., D'Eugenio, F., Souchereau, H., and Ferreira, L., "astropy/photutils: 1.0.0," (Sept. 2020).

[30] Wang, L., Macri, L. M., Wang, L., Ashley, M. C. B., Cui, X., Feng, L.-L., Gong, X., Lawrence, J. S., Liu, Q., Luong-Van, D., Pennypacker, C. R., Shang, Z., Storey, J. W. V., Yang, H., Yang, J., Yuan, X., York, D. G., Zhou, X., Zhu, Z., and Zhu, Z., "Photometry of Variable Stars from Dome A, Antarctica: Results from the 2010 Observing Season," *Astronomical Journal* **146**, 139 (Dec. 2013).

[31] Oelkers, R. J., Macri, L. M., Wang, L., Ashley, M. C. B., Cui, X., Feng, L.-L., Gong, X., Lawrence, J. S., Qiang, L., Luong-Van, D., Pennypacker, C. R., Yang, H., Yuan, X., York, D. G., Zhou, X., and Zhu, Z., "Difference Image Analysis of Defocused Observations With CSTAR," *Astronomical Journal* **149**, 50 (Feb. 2015).

[32] Oelkers, R. J. and Stassun, K. G., "Precision Light Curves from TESS Full-frame Images: A Difference Imaging Approach," *Astronomical Journal* **156**, 132 (Sept. 2018).

[33] Duchon, J., "Interpolation des fonctions de deux variables suivant le principe de la flexion des plaques minces," *ESAIM: Mathematical Modelling and Numerical Analysis - Modélisation Mathématique et Analyse Numérique* **10**(R3), 5–12 (1976).

[34] Vanderburg, A. and Johnson, J. A., "A Technique for Extracting Highly Precise Photometry for the Two-Wheeled Kepler Mission," *Publ. Astron. Soc. Pac.* **126**, 948 (Oct. 2014).